# A smart model to estimate effective thermal conductivity and viscosity in the weld pool

A. De and T. DebRoy[a)]
*Department of Materials Science and Engineering, The Pennsylvania State University, University Park, Pennsylvania 16802*

(Received 28 August 2003; accepted 12 February 2004)

Calculations of fluid flow and heat transfer in the weld pool are strongly influenced by the values of effective thermal conductivity and effective viscosity of the liquid metal. The values of these variables are uncertain since the welding conditions and the fluid flow characteristics within the weld pool influence them. Following an inverse modeling approach, the present work develops a smart model that embodies a multivariable optimization scheme within the framework of a phenomenological heat transfer and fluid flow model to estimate the uncertain parameters necessary for weld pool modeling. The optimization scheme considers the sensitivity of the calculated weld geometry with respect to the unknown parameters. To avoid unrealistic optimized solutions, the smart model is internally guided to look for only the physically significant solutions. The model could estimate the effective thermal conductivity and effective viscosity for conduction mode laser welding as a function of nondimensional heat input from six sets of experimental measurements of weld pool depth and width. © *2004 American Institute of Physics.* [DOI: 10.1063/1.1695593]

## I. INTRODUCTION

Investigations of heat and mass transfer in the weld pool are important for understanding fusion welding processes and welded materials.[1–3] Direct experimental measurement of temperature and velocity fields in the weld pool is a difficult task and such measurements are restricted to the weld pool surface in most cases. A recourse is to numerically solve the equations of conservation of mass, momentum, and energy to systematically study weld characteristics such as thermal cycles and weld pool dimensions.[4–7] The computed thermal cycles can be further used to quantitatively understand weld metal phase composition,[8–10] grain structure,[10,11] inclusion structure,[12–14] and weld metal composition changes owing to both vaporization of alloying elements[15,16] and dissolution of gases.[17,18] Although the numerical simulation models have been extensively used as a research tool,[19–23] their use for designing and manufacturing activities in the industry has been rather limited. An important difficulty is that these models need many input parameters some of which cannot be accurately prescribed from fundamental principles.[2,24]

Values of variables related to the workpiece geometry, welding parameters, and material properties are necessary for numerical calculations of heat transfer and fluid flow in the weld pool. In the case of laser welding, several of these parameters such as the laser power, spot diameter, and welding speed can be specified with a reasonable degree of certainty. However, the values of effective thermal conductivity and the effective viscosity cannot be determined from fundamental principles.[2,24–28] Values of these variables are important, since they allow modeling of the high rates of transport of heat, mass, and momentum in systems with strong fluctuating velocities that are inevitable in small weld pools with very strong convection currents. Enhanced values of liquid thermal conductivity and viscosity[2,24–28] have been frequently used as effective values in consideration of the fluctuating components of velocities in the weld pool. Alternatively, the two-equation $k-\epsilon$ turbulence model has also been used in estimating effective viscosity and effective thermal conductivity in the weld pool.[24,29] However, the two-equation $k-\epsilon$ turbulence model contains empirical constants that were originally developed to model parabolic fluid flow in large systems such as large pipes. Since the effective thermal conductivity and viscosity are system properties, in this work their values are determined from the combination of a heat transfer and fluid flow model, an optimization algorithm,[25,26,29] and a limited volume of experimentally measured weld pool dimensions for various welding conditions.

The optimization procedure attempts to estimate the unknown parameters from the sensitivity of the known input variables with respect to the unknown parameters. The sensitivity terms are calculated by running the heat transfer and fluid flow model several times for small changes in the unknown parameters. The computationally intensive nature of

TABLE I. Measured weld dimensions and welding parameters (see Ref. 35).

| Data set index | Laser power (W) | Weld velocity (mm $s^{-1}$) | Absorptivity | Spot radius (mm) | Weld penetration (mm) | Weld width (mm) |
|---|---|---|---|---|---|---|
| 1 | 3500 | 8.33 | 0.30 | 1.3 | 1.00 | 4.00 |
| 2 | 5000 | 3.33 | 0.13 | 1.3 | 1.10 | 4.00 |
| 3 | 5000 | 8.33 | 0.30 | 1.3 | 1.25 | 5.25 |
| 4 | 3200 | 3.33 | 0.30 | 1.4 | 1.75 | 4.00 |
| 5 | 4800 | 3.33 | 0.30 | 1.4 | 2.50 | 6.00 |
| 6 | 5000 | 3.33 | 0.30 | 1.3 | 2.25 | 6.75 |

a)Electronic mail: debroy@psu.edu

 

TABLE II. Chemical composition (wt %) of steel used for welding experiments (for data set index 1, 2, 3, and 6) (see Ref. 35).

| C | Cr | W | Mo | V | Co | Mn |
|---|---|---|---|---|---|---|
| 0.92 | 3.88 | 6.08 | 4.9 | 1.73 | 0 | 0.26 |
| Si | S | Ni | P | Cu | Al | Fe |
| 0.23 | 0.001 | 0.24 | 0.024 | 0.20 | 0.019 | Bal. |

these calculations has clearly affected similar efforts in the past.[30–34] These efforts completely ignored convection in the weld pool and were based on heat conduction equations.[33,34] Recent advances in computational hardware and software now permit optimization calculations that consider heat transfer and fluid flow in three dimensions. The approach adopted here is inherently different from a neural network technique where the input and output variables are related through a set of hidden nodes and their relationships do not have to comply with any physical law. In the research reported in this article, the input welding parameters and the output weld pool geometry are related by a phenomenological framework of the equations of conservation of mass, momentum, and energy. In effect, the complete procedural scheme acts as a smart model that identifies a few unknown parameters in an iterative manner starting from a set of their initial guessed values exploiting the phenomenological framework.

Values of effective thermal conductivity and effective viscosity are estimated through a combination of the Levenburg–Marquardt method of nonlinear parameter optimization, a numerical heat transfer and fluid flow model, and a set of experimentally measured weld pool dimensions. The optimization algorithm minimizes the error between the predicted and the experimentally observed penetration and the weld width included in Table I for six laser welds.[35] The chemical compositions of the steels used are presented[35] in Tables II and III. The thermophysical properties used in the calculations are given[35] in Tables IV and V. The welding conditions presented in Table III show various values of laser power, spot diameter, absorptivity, and welding speed used. In order to include these variations, a nondimensional representation of the effective heat input that considers the combined contribution of the laser beam characteristics (e.g., laser power and the spot size) and welding parameters (e.g., welding speed) is formed as

$$N_{\mathrm{HI}}=\frac{\dfrac{P\eta}{\pi r_b^2\cdot v}}{\rho C_{PS}(T_L-T_a)+\rho L}, \tag{1}$$

TABLE III. Chemical composition (wt %) of steel used for welding experiments (for data set index 4 and 5) (see Ref. 35).

| C | Cr | W | Mo | V | Co | Mn |
|---|---|---|---|---|---|---|
| 0.21 | 0.21 | <0.05 | 0.05 | <0.02 | <0.05 | 1.52 |
| Si | S | Ni | P | Cu | Al | Fe |
| 0.36 | 0.006 | 0.14 | <0.005 | 0.14 | 0.01 | Bal. |

TABLE IV. Data used for calculations of temperature and velocity fields (for data set index 1, 2, 3, and 6) (see Ref. 35).

| Physical property | Value |
|---|---|
| Liquidus temperature, $T_L$ (K) | 1700.0 |
| Solidus temperature, $T_S$ (K) | 1480.0 |
| Ambient temperature, $T_a$ (K) | 293.0 |
| Density of liquid metal, $\rho$ (kg/m$^3$) | $8.1\times10^3$ |
| Thermal conductivity of solid, $k_S$ (W m$^{-1}$ K$^{-1}$) | 25.08 |
| Thermal conductivity of liquid, $k_L$ (W m$^{-1}$ K$^{-1}$) | 25.08 |
| Specific heat of solid, $C_{\mathrm{PS}}$ (J kg$^{-1}$ K$^{-1}$) | 711.0 |
| Specific heat of liquid, $C_{\mathrm{PL}}$ (J kg$^{-1}$ K$^{-1}$) | 711.0 |
| Temperature coefficient of surface tension, $d\gamma/dT$ (N m$^{-1}$ K$^{-1}$) | $-0.5\times10^{-3}$ |
| Coefficient of thermal expansion, $\beta$ (K$^{-1}$) | $1.5\times10^{-6}$ |
| Viscosity of molten iron at 1823 K, $\mu_{\mathrm{fl}}$ (kg m$^{-1}$ s$^{-1}$) | $6.7\times10^{-3}$ |

where $P$ is the laser power (W), $\eta$ is the absorptivity, $r_b$ is the spot radius (m), $v$ is the weld velocity (m s$^{-1}$), $C_{PS}$ is the specific heat of solid metal (J kg$^{-1}$ K$^{-1}$), $\rho$ is the density (kg m$^{-3}$), $L$ is the latent heat of fusion (J kg$^{-1}$) and $T_L$ and $T_a$ are the liquidus and ambient temperatures (K), respectively. In Eq. (1), the numerator represents the absorbed heat per unit volume and the denominator depicts the change in the enthalpy required to heat a unit volume of the metal from ambient temperature to liquidus temperature. The computed values of $N_{\mathrm{HI}}$ for different welds are given in Table VI.

## II. HEAT TRANSFER AND FLUID FLOW SIMULATION

The flow of liquid metal in the weld pool in three dimensional Cartesian coordinate system is represented by the following momentum conservation equation:[4,21,22,36]

$$\rho\frac{\partial u_j}{\partial t}+\rho\frac{\partial(u_iu_j)}{\partial x_i}=\frac{\partial}{\partial x_i}\left(\mu\frac{\partial u_j}{\partial x_i}\right)+S_j, \tag{2}$$

where $\rho$ is the density, $t$ is the time, $x_i$ is the distance along the $i=1$, 2, and 3 directions, $u_j$ is the velocity component along the $j$ direction, $\mu$ is the effective viscosity, and $S_j$ is the source term for the $j$th momentum equation and is given as[21,22]

$$S_j=-\frac{\partial p}{\partial x_j}+\frac{\partial}{\partial x_j}\left(\mu\frac{\partial u_j}{\partial x_j}\right)-C\left[\frac{(1-f_L)^2}{f_L^3+B}\right]u_j+Sb_j, \tag{3}$$

TABLE V. Data used for calculations of temperature and velocity fields (for data set index 4 and 5) (see Ref. 35).

| Physical property | Value |
|---|---|
| Liquidus temperature, $T_L$ (K) | 1800.0 |
| Solidus temperature, $T_S$ (K) | 1760.0 |
| Ambient temperature, $T_a$ (K) | 293.0 |
| Density of liquid metal, $\rho$ (kg/m$^{-1}$) | $7.2\times10^3$ |
| Thermal conductivity of solid, $k_S$ (W m$^{-1}$ K$^{-1}$) | 25.08 |
| Thermal conductivity of liquid, $k_L$ (W m$^{-1}$ K$^{-1}$) | 25.08 |
| Specific heat of solid, $C_{\mathrm{PS}}$ (J kg$^{-1}$ K$^{-1}$) | 754.0 |
| Specific heat of liquid, $C_{\mathrm{PL}}$ (J kg$^{-1}$ K$^{-1}$) | 754.0 |
| Temperature coefficient of surface tension, $d\gamma/dT$ (N m$^{-1}$ K$^{-1}$) | $-0.5\times10^{-3}$ |
| Coefficient of thermal expansion, $\beta$ (K$^{-1}$) | $1.5\times10^{-6}$ |
| Viscosity of molten iron at 1823 K, $\mu_{\mathrm{fl}}$ (kg m$^{-1}$ s$^{-1}$) | $6.7\times10^{-3}$ |

TABLE VI. Nondimensional value related to heat input.

| Data set index | Laser power (W) | Weld velocity (mm s$^{-1}$) | Absorptivity | Spot radius (mm) | $N_{HI}$ |
|---|---|---|---|---|---|
| 1 | 3500 | 8.33 | 0.30 | 1.3 | 2.9 |
| 2 | 5000 | 3.33 | 0.13 | 1.3 | 4.1 |
| 3 | 5000 | 8.33 | 0.30 | 1.3 | 4.5 |
| 4 | 3200 | 3.33 | 0.30 | 1.4 | 6.6 |
| 5 | 4800 | 3.33 | 0.30 | 1.4 | 9.9 |
| 6 | 5000 | 3.33 | 0.30 | 1.3 | 10.4 |

where $p$ is the pressure, $f_L$ is the liquid fraction, $B$ is a constant introduced to avoid division by zero, and $C(=1.6\times10^4)$ is a constant that takes into account mushy zone morphology, and $Sb_j$ represents both the electromagnetic and buoyancy source terms. The third term on the right-hand side represents the frictional dissipation in the mushy zone according to the Carman–Kozeny equation for flow through a porous media.[37,38] The value of the effective viscosity in Eq. (2) is a property of the specific welding system and not a physical property of the liquid metal. Typical values of effective viscosity are much higher than that of the molecular viscosity.[25,28,29,39] The higher value is important, since it allows accurate modeling of the high rates of transport of momentum in systems with strong fluctuating velocities that are inevitable in small weld pools with very strong convection currents.[25,28] The pressure field was obtained by solving the following continuity equation simultaneously with the momentum equation:

$$\frac{\partial(\rho u_i)}{\partial x_i}=0. \tag{4}$$

The total enthalpy $H$ is represented by a sum of sensible heat $h$ and latent heat content $\Delta H$, i.e., $H=h+\Delta H$ where $h=\int C_p dT$, $C_p$ is the specific heat, $T$ is the temperature, $\Delta H=f_L L$, $L$ is the latent heat of fusion, and the liquid fraction $f_L$ is assumed to vary linearly with temperature in the mushy zone[4]

$$f_L=\begin{cases}1 & T>T_L\\ \dfrac{T-T_S}{T_L-T_S} & T_S\leqslant T\leqslant T_L,\\ 0 & T<T_S\end{cases} \tag{5}$$

where $T_L$ and $T_S$ are the liquidus and solidus temperature, respectively. The thermal energy transport in the weld workpiece can be expressed by the following modified energy equation:[34]

$$\rho\frac{\partial h}{\partial t}+\rho\frac{\partial(u_i h)}{\partial x_i}=\frac{\partial}{\partial x_i}\left(\frac{k}{C_p}\frac{\partial h}{\partial x_i}\right)-\rho\frac{\partial(\Delta H)}{\partial t}-\rho\frac{\partial(u_i\Delta H)}{\partial x_i}, \tag{6}$$

where $k$ is the thermal conductivity. In the liquid region, the value of the thermal conductivity in Eq. (6) is taken as the effective thermal conductivity which is a property of the specific welding system and not a physical property of the liquid metal. Typical values of effective thermal conductivity are much higher than that of the thermal conductivity of the liquid. The higher value is important, since it allows accurate modeling of the high rates of transport of heat in systems with strong fluctuating velocities that are inevitable in small weld pools with very strong convection currents.[39] Since the weld is symmetrical about the weld center line only half of the workpiece is considered. The weld top surface is assumed to be flat. The velocity boundary condition is given as[4]

$$\mu\frac{\partial u}{\partial z}=f_L\frac{d\gamma}{dT}\frac{\partial T}{\partial x},\qquad \mu\frac{\partial v}{\partial z}=f_L\frac{d\gamma}{dT}\frac{\partial T}{\partial y},\qquad w=0, \tag{7}$$

where $u$, $v$, and $w$ are the velocity components along the $x$, $y$, and $z$ directions, respectively, and $d\gamma/dT$ is the temperature coefficient of surface tension. As shown in Eq. (7), the $u$ and $v$ velocities are determined from the Marangoni effect. The $w$ velocity is equal to zero since there is no flow of liquid metal perpendicular to the pool top surface. The heat flux at the top surface is given as

$$k\frac{\partial T}{\partial z}=\frac{dP\eta}{\pi r_b^2}\exp\left[-\frac{d(x^2+y^2)}{r_b^2}\right]-\sigma\epsilon(T^4-T_a^4)-h_c(T-T_a), \tag{8}$$

where $r_b$ is the laser beam radius, $d$ is the beam distribution factor, $P$ is the laser beam power, $\eta$ is the absorptivity, $\sigma$ is the Stefan–Boltzmann constant, $h_c$ is the heat transfer coefficient, and $T_a$ is the ambient temperature. The first term on the right-hand side is the heat input from the heat source, defined by a Gaussian heat distribution. The second and third terms represent the heat loss by radiation and convection, respectively. The boundary conditions are defined as zero flux across the symmetric surface (i.e., at $y=0$) as[4,21]

$$\frac{\partial u}{\partial y}=0,\quad v=0,\quad \frac{\partial w}{\partial y}=0, \tag{9}$$

$$\frac{\partial h}{\partial y}=0. \tag{10}$$

At all other surfaces, temperatures are set at ambient temperature and the velocities are set to be zero.

## III. OPTIMIZATION PROCEDURE

Optimization algorithms commonly utilized for parameter estimation include the Levenberg–Marquardt method, conjugate gradient technique, and conjugate gradient method with adjoint problem. These methods have been discussed elsewhere.[40–42] The Levenberg–Marquardt method involves minimization of an appropriately constructed objective function that depicts the error between the estimated and the corresponding known values of dependent variables. The iterative solution procedure resembles the typical nonlinear least square technique and is principally dependent on the sensi-

tivity of the dependent variables to the unknown independent variables. The conjugate gradient technique is similar to the Levenberg–Marquardt method in the aspects of the objective function and sensitivity calculation. However, the iterative procedure in conjugate gradient technique involves the calculation of a suitable step size for each iteration along a direction of descent. The direction of descent is obtained as a linear combination of the negative gradient direction at the current iteration and the same obtained in the previous iteration. The conjugate gradient method with adjoint problem is utilized if the unknown parameters can be expressed in terms of the coefficients of a known trial function. This method uses a Lagrange multiplier, and does not require calculation of the sensitivity matrix that is inherent in both the previous methods. Although both the Levenberg–Marquardt method and the conjugate gradient technique are suitable for the problem considered in the present work, the first one has been adopted here. The suitability of the Levenberg–Marquardt method for the optimization of multiple unknown variables in the case of gas tungsten arc welding process has already been reported in a previous work.[27]

The Levenberg–Marquardt optimization technique minimizes an objective function that depicts the difference between the computed and measured values of one or more dependent or target variables. Considering the penetration and the width of the weld pool as the dependent variables, an objective function, $O(f)$, is defined as

$$O(f)=\sum_{m=1}^{M}\left(\frac{p_m^c-p_m^{\mathrm{obs}}}{p_m^{\mathrm{obs}}}\right)^2+\sum_{m=1}^{M}\left(\frac{w_m^c-w_m^{\mathrm{obs}}}{w_m^{\mathrm{obs}}}\right)^2 =\sum_{m=1}^{M}(p_m^*-1)^2+\sum_{m=1}^{M}(w_m^*-1)^2, \tag{11}$$

where $p_m^c$ and $w_m^c$ are the penetration and the width of the weld pool calculated by the numerical heat transfer and fluid flow model, respectively, and $p_m^{\mathrm{obs}}$ and $w_m^{\mathrm{obs}}$ are the corresponding experimental measurements. $p_m^*$ and $w_m^*$ are nondimensional and indicate the extent of over- or underprediction for penetration and weld width, respectively. The subscript $m$ in each of the variables in Eq. (11) corresponds to a specific weld in a series of $M$ number of total welds ($M=6$, Table I). In Eq. (11), $f$ represents a given set of independent unknown parameters, which strongly influence the dependent variables, $p_m^*$ and $w_m^*$, and hence, the objective function, $O(f)$. In the present work, $f$ consists of effective thermal conductivity and effective viscosity of the liquid metal (in weld pool) taken in nondimensional form

$$\{f\}\equiv\{f_1\ \ f_2\}\equiv\{k^*\ \ \mu^*\}\equiv\left\{\frac{k_{\mathrm{eff}}}{k_L}\ \ \frac{\mu_{\mathrm{eff}}}{\mu_{\mathrm{fl}}}\right\}. \tag{12}$$

In Eq. (12), $k_L$, $\mu_{\mathrm{fl}}$, $k_{\mathrm{eff}}$, and $\mu_{\mathrm{eff}}$, respectively, refer to thermal conductivity of liquid metal at melting temperature, viscosity of molten iron at 1823 K, effective thermal conductivity, and effective viscosity of liquid metal in weld pool. Assuming that $O(f)$ is continuous and has a minimum value, the optimum values of the two unknowns are obtained by differentiating Eq. (11) with respect to each unknown parameter and equating each of the derivatives to zero

$$\left[\frac{\partial O(f)}{\partial f_i}\right]_{i=1,2}=2\left[\sum_{m=1}^{M}(p_m^*-1)\frac{\partial p_m^*}{\partial f_i}+\sum_{m=1}^{M}(w_m^*-1)\frac{\partial w_m^*}{\partial f_i}\right]_{i=1,2}=0, \tag{13}$$

where $f_i$ represents any one of the two unknowns as indicated in Eq. (12). The partial derivatives of $p_m^*$ and $w_m^*$ with respect to $f_i$ in Eq. (13) are generally referred to as the sensitivity of the computed weld width and penetration with respect to the unknowns. The values of these sensitivity terms are computed numerically by running the numerical heat transfer and fluid flow code and subsequently, calculating the derivatives. For example, the sensitivity of nondimensional penetration, $p_m^*$, with respect to $k^*$, is calculated from the following relation:

$$\frac{\partial p_m^*}{\partial k^*}=\frac{p_m^*(k^*+\delta k^*,\mu^*,\text{other known parameters})-p_m^*(k^*,\mu^*,\text{other known parameters})}{\delta k^*}, \tag{14}$$

where $\delta k^*$ is very small compared with $k^*$. The expression (14) indicates that computation of each sensitivity term needs two executions of the numerical heat and fluid flow analysis.

Thus, the optimization procedure, and in turn, the overall smart model, intends to solve Eq. (13) to obtain a specific solution of the unknown parameters. In other words, the optimization routine targets to achieve the final set of $k^*$ and $\mu^*$ using which the computed $p_m^c$ and $w_m^c$ will be sufficiently close to the corresponding $p_m^{\mathrm{obs}}$ and $w_m^{\mathrm{obs}}$ for all $M$ sample welds. Eventually, both $p_m^*$ and $w_m^*$ will move close to 1 and Eq. (13) will thus be satisfied. However, $p_m^c$ and $w_m^c$ in Eq. (13) are obtained from the solution of the numerical heat transfer and fluid flow model for a certain set of $k^*$ and $\mu^*$, and these unknown parameters do not explicitly appear in Eq. (13). Hence, this equation cannot provide a direct solution for $k^*$ and $\mu^*$. As shown in the appendix, considerable rearrangements of the equations are necessary so that they can serve as a basis for an iterative scheme to evaluate the unknown parameters, $k^*$ and $\mu^*$. The final equations take the following form:

$$[S]\{\Delta f^k\}=-\{S^*\}, \tag{15}$$

where $\Delta f^k$ are the increments of the $f$ values after $k$ iteration;

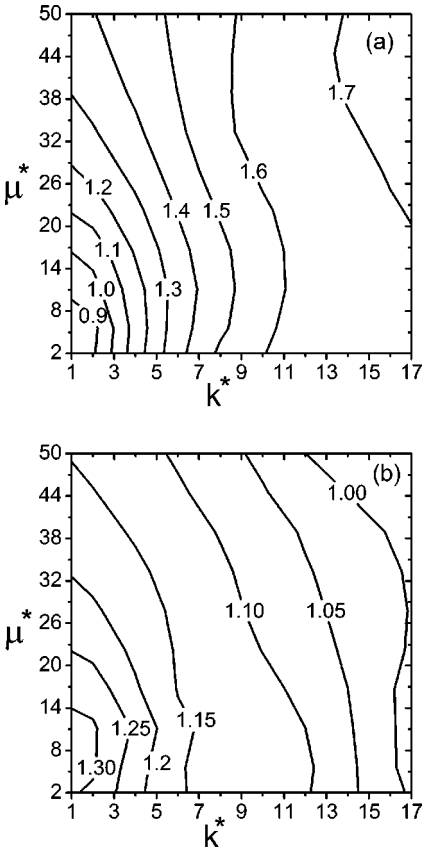


FIG. 1. Influence of $k^*$ and $\mu^*$ on (a) $p_m^*$ and (b) $w_m^*$. Welding parameters: $P=3500$ W, $\eta=0.30$, $v=8.33$ mm/s ($N_{\mathrm{HI}}=2.9$).

$[S]$ and $\{S^*\}$ are defined in the appendix by Eqs. (A16) and (A17), respectively. The iterations are continued until the objective function defined by Eq. (11) is minimized. The solution methodology is discussed in details in the appendix.

## IV. RESULTS AND DISCUSSION

The sensitivity of the computed weld pool dimensions with $k^*$ and $\mu^*$ was studied for each of the six welding conditions presented in Table I. Several heat transfer and fluid flow calculations were carried out with different combinations of $k^*$ and $\mu^*$ for each set of welding conditions. Figures 1(a) and 1(b) show a number of isocontours of $p_m^*$ and $w_m^*$, respectively, as a function of $k^*$ and $\mu^*$ corresponding to the first data set in Table I. It is observed in Fig. 1(a) that $p_m^*$ increases as $k^*$ or $\mu^*$ increases. The increasing trend in $p_m^*$ with $k^*$ dampens slowly when $k^*$ is increased beyond a value of 7.0. Similarly, as $k^*$ increases beyond a value of 5.0, $p_m^*$ becomes almost insensitive to $\mu^*$. Figure 1(b) depicts that $w_m^*$ decreases as $k^*$ or $\mu^*$ increases. As $k^*$ increases beyond 7.0, $w_m^*$ becomes almost insensitive to $\mu^*$ and the influence of $k^*$ on $w_m^*$ reduces considerably.

The influence of $k^*$ and $\mu^*$ on the computed weld pool dimensions can be explained as follows. An increase in $k^*$ promotes higher heat conduction within the weld pool. The dimensionless penetration $p_m^*$ increases with increase in $k^*$ because higher thermal conductivity facilitates heat transport in the downward direction. However, the higher the enhanced thermal conductivity, the lower will be the resulting surface temperature gradient. Consequently, the radial convective heat transport is decreased resulting in decreased $w_m^*$ at higher $k^*$. On the other hand, an increase in $\mu^*$ reduces surface velocity, since a more viscous fluid flows slowly under the same driving force. The reduced surface velocity leads to lower radial convective heat transfer, lower computed weld width, and slightly higher peak temperature. The increase in peak temperature enhances downward heat conduction and leads to slightly higher computed penetration, $p_m^*$. At high values of $k^*$, conduction is the main mechanism of heat transfer and a change in $\mu^*$ cannot significantly alter the surface velocity or the peak temperature. Thus, the computed penetration or weld width do not change significantly with $\mu^*$ at high values of $k^*$ as observed in Figs. 1(a) and 1(b).

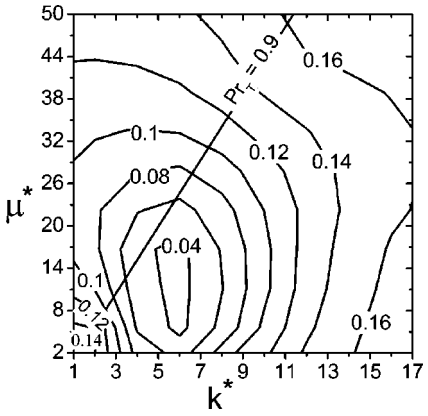


FIG. 2. Influence of $k^*$ and $\mu^*$ on $O(f)$. Welding parameters: $P=3500$ W, $\eta=0.30$, $v=8.33$ mm/s ($N_{\mathrm{HI}}=2.9$).

Figures 1(a) and 1(b) show that unit values $p_m^*$ and $w_m^*$ can be achieved with multiple combinations of $\mu^*$ and $k^*$. The values of the error in nondimensional, $O(f)$ is plotted next in Fig. 2 as a function of $\mu^*$ and $k^*$. Figure 2 indicates that a specific combination of $\mu^*$ and $k^*$ to achieve minimum values of $O(f)$. However, two features are to be noted here. Figure 2 represents a heat input of $N_{\mathrm{HI}}=2.9$ in Table VI. There is no guarantee that the same combination of $\mu^*$ and $k^*$ will lead to a minimum error corresponding to other values of $N_{\mathrm{HI}}$. Considering the selected combinations of $\mu^*$ and $k^*$, the turbulent Prandtl number may be defined as

$$\mathrm{Pr}_r=\frac{\mu_T C_{\mathrm{PL}}}{k_T}, \tag{16}$$

where $\mu_{\mathrm{eff}}=\mu_{\mathrm{fl}}+\mu_T$ and $k_{\mathrm{eff}}=k_L+k_T$; $\mu_T$ and $k_T$ are the turbulent viscosity and conductivity to account for the fluctuating fluid velocity within the weld pool. Since $\mathrm{Pr}_T$ is commonly[24,25] prescribed as 0.9, a dashed line is plotted in Fig. 2 corresponding to $\mathrm{Pr}_T=0.9$. This line provides an additional guideline for the selection of solutions.

Figure 3 presents values of the objective function, $O(f)$, as a function of $\mu^*$ and $k^*$ corresponding to $N_{\mathrm{HI}}=9.87$ along with a dashed line representing $\mathrm{Pr}_T=0.9$. Comparison of Figs. 2 and 3 show that in order to accurately calculate weld dimensions, higher values of $\mu^*$ and $k^*$ are needed at higher heat inputs. Similar calculations for other values of $N_{\mathrm{HI}}$ further confirm this trend. The calculations demonstrate the un-

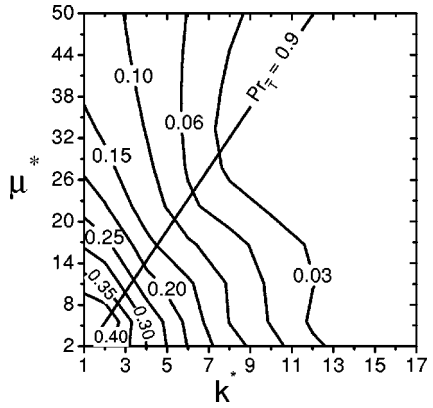


FIG. 3. Influence of $k^*$ and $\mu^*$ on $O(f)$. Welding parameters: $P = 4800$ W, $\eta = 0.30$, $v = 3.33$ mm/s ($N_{HI} = 9.9$).

derlying principle that $\mu^*$ and $k^*$ in weld pool are dependent on heat input. Their values depend on the welding conditions rather than the nature of the liquid metal. The values of $k^*$ and $\mu^*$ can be expressed as

$$k^* = C_1 + C_2 \ N_{HI},$$
$$\mu^* = C_3 + C_4 \ N_{HI}, \tag{17}$$

where $C_1$ and $C_3$ are the minimum values of the effective conductivity and effective viscosity, respectively, and $C_2$ and $C_4$ constants. Thus, the objective function, $O(f)$, is now a function of $C_1$, $C_2$, $C_3$, and $C_4$ as they will determine a specific set of $k^*$ and $\mu^*$ for a specific heat input. Furthermore, since $k^*$ and $\mu^*$ equals 1 at low values of heat input, values of both $C_1$ and $C_3$ are one. The optimization routine can be used to estimate the most suitable values of $C_2$ and $C_4$ that will provide a set of $k^*$ and $\mu^*$ for each $N_{HI}$. Hence, Eq. (12) is modified as

$$\{f\} \equiv \{f_1 \ \ f_2\} \equiv \{C_2 \ \ C_4\}. \tag{18}$$

Furthermore, the optimization routine will be guided by the fact that the desired set of $k^*$ and $\mu^*$ for each $N_{HI}$ should have a $Pr_T$ close to 0.9.

To start the optimization calculation, a set of initial guessed values are necessary for $C_2$ and $C_4$. The final results were not affected by the choice of the initial guessed values. The values of these three sets of initial guessed values for $C_2$ and $C_4$ and the corresponding initial values of $k^*$ and $\mu^*$ are presented in Table VII. Figures 4–6 show the results of the

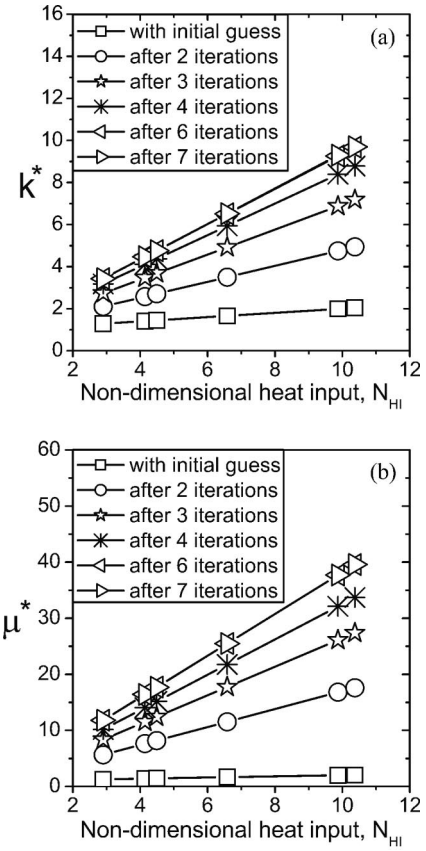


FIG. 4. Progress of calculation with first set of initial guessed values. The guessed values are presented in Table VII.

calculations for three sets of initial guessed values and Fig. 7 shows that how, $O(f)$, the error, reduces with number of iterations. In Figs. 4–6, instead of presenting the changes in values of $C_2$ and $C_4$ with a number of iterations, the corresponding patterns in $k^*$ and $\mu^*$ with respect to $N_{HI}$ are plotted at different iterations. Figure 4(a) and 4(b) show how $k^*$ and $\mu^*$ change with $N_{HI}$ after various iterations. The linearly increasing trend in both cases stabilizes after about six iterations. The values of $k^*$ range from 3.4 at $N_{HI} = 2.9$ to a value of 9.7 at $N_{HI} = 10.4$. The corresponding values of $\mu^*$ are set from 11.8 at $N_{HI} = 2.9$ to a value of 39.6 at $N_{HI} = 10.4$. The stabilization of error with the initial guessed values after six iterations is also evident in Fig. 7. Similarly, Figs. 5(a) and 5(b) depict the trends in $k^*$ and $\mu^*$ with respect to $N_{HI}$ at

TABLE VII. Final values of $k^*$ and $\mu^*$ for all data sets with different initial guesses.

| Data set index | Initial guess (1st set) | | Initial guess (2nd set) | | Initial guess (3rd set) | | Final values | |
|---|---|---|---|---|---|---|---|---|
| | $C_2$:0.1; $C_4$:0.1 | | $C_2$:1.0; $C_4$:1.0 | | $C_2$:2.0; $C_4$:2.0 | | $C_2$:0.84; $C_4$:3.72 | |
| | $k^*$ | $\mu^*$ | $k^*$ | $\mu^*$ | $k^*$ | $\mu^*$ | $k^*$ | $\mu^*$ |
| 1 | 1.29 | 1.29 | 3.90 | 3.90 | 6.80 | 6.80 | 3.43 | 11.80 |
| 2 | 1.41 | 1.41 | 5.14 | 5.14 | 9.29 | 9.29 | 4.47 | 16.40 |
| 3 | 1.45 | 1.45 | 5.49 | 5.49 | 9.98 | 9.98 | 4.76 | 17.71 |
| 4 | 1.66 | 1.66 | 7.58 | 7.58 | 14.16 | 14.16 | 6.52 | 25.48 |
| 5 | 1.99 | 1.99 | 10.87 | 10.87 | 20.74 | 20.74 | 9.29 | 37.72 |
| 6 | 2.04 | 2.04 | 11.37 | 11.37 | 21.73 | 21.73 | 9.70 | 39.58 |

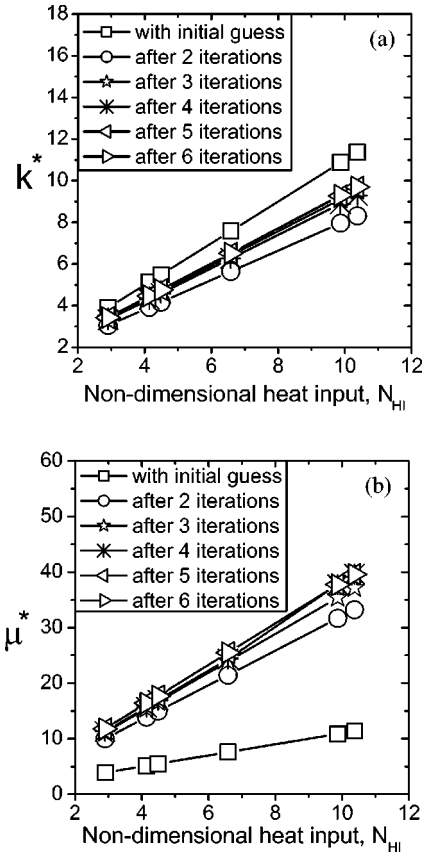


FIG. 5. Progress of calculation with second set of initial guessed values. The guessed values are presented in Table VII.

different iterations with the second set of initial guessed values. The final trends in both $k^*$ and $\mu^*$ have remained same as obtained previously. Both Figs. 5(a) and 5(b) show no changes in the trends of $k^*$ and $\mu^*$ after four iterations. Figure 6 shows that with the third set of initial guessed values, the trends in $k^*$ and $\mu^*$ with respect to $N_{\mathrm{HI}}$ at different iterations and the final values of $k^*$ and $\mu^*$ for different values of $N_{\mathrm{HI}}$ remain same as previous. Figures 6 and 7 also indicate that the optimum solution with the third set of initial guessed values is achieved after four iterations after which the error does not improve. The final values of $C_2$ and $C_4$ as

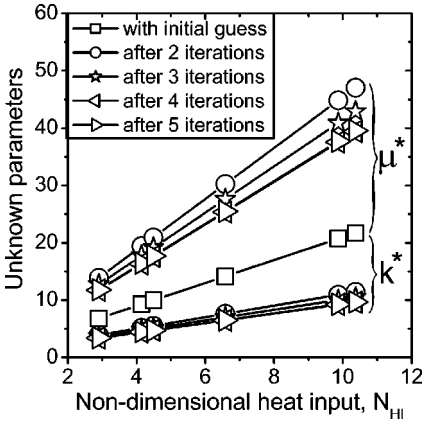


FIG. 6. Progress of calculation with third set of initial guessed values. The guessed values are presented in Table VII.

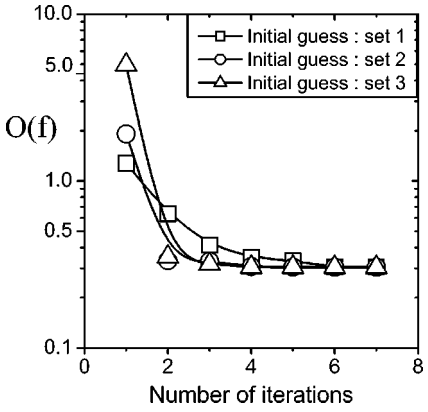


FIG. 7. Progress of $O(f)$ with three sets of initial guessed values. The guessed values are presented in Table VII.

well as the corresponding combinations of $k^*$ and $\mu^*$ for each $N_{\mathrm{HI}}$ are presented in Table VII. $\mathrm{Pr}_T$ in each case also remains close to 0.9. The final form of Eq. (17) can be presented as

$$k^* = 1.0 + 0.84\ N_{\mathrm{HI}},$$
$$\mu^* = 1.0 + 3.72\ N_{\mathrm{HI}}. \tag{19}$$

The choice of initial values did not affect how $k^*$ and $\mu^*$ varied with $N_{\mathrm{HI}}$. However, the initial values affected the total number of iterations needed to achieve converged solution. It is useful to look into the number of heat transfer and fluid flow analyses needed per iteration. The number of runs is equivalent to the number of unknowns multiplied by the number of sample welds (for sensitivity calculation) plus the number of welds (for error verification). Therefore, it is useful to reduce even a single iteration by appropriate choice of the initial guessed values. The computed values of $p_m^*$ and $w_m^*$ using the optimized values for $k^*$ and $\mu^*$ corresponding to all values of $N_{\mathrm{HI}}$ are next plotted in Fig. 8. Although a fairly satisfactory agreement is obtained between the computed and measured weld dimensions, the weld dimensions are slightly overpredicted for the material composition presented in Table II. It can be observed from Figs. 1(a) and 1(b) that $p_m^*$ tends to be one at lower values of $k^*$ and $\mu^*$

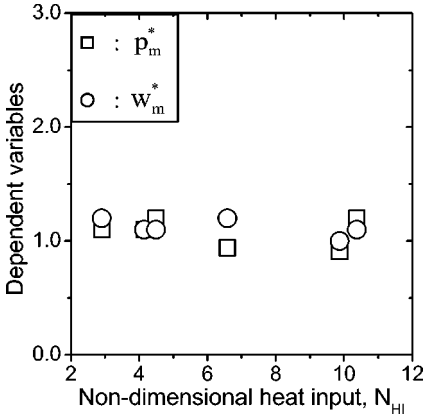


FIG. 8. Computed values of $p_m^*$ and $w_m^*$ using the optimized set of $k^*$ and $\mu^*$ for all values of $N_{\mathrm{HI}}$. Data used in the calculation are given in Tables IV, V, and VII.

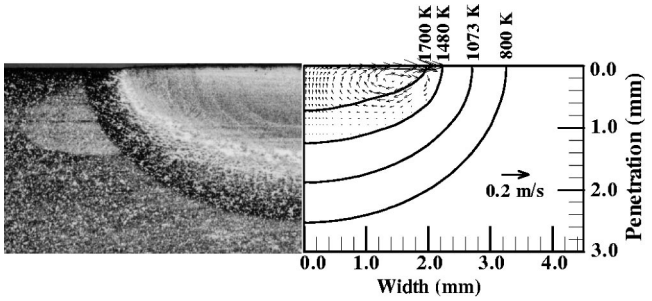


FIG. 9. Experimentally determined and computed weld pool geometry. The length of the black arrow shows the magnitude of the velocities and the solid lines show the isotherms. Welding parameters: $P=3500$ W, $\eta=0.30$, and $v=8.33$ mm/s ($N_{HI}=2.9$); Other data used in the calculations are given in Tables IV and VII.

while $w_m^*$ tends to be 1 at higher values of $k^*$ and $\mu^*$ and both $p_m^*$ and $w_m^*$ are slightly higher than 1 for intermediate values. Although the smart model attempts to find the total composite error, since the relations between weld dimensions with $k^*$ and $\mu^*$ are not linear, the errors in both $p_m^*$ and $w_m^*$ may not be equal in magnitude.

A comparison between the computed weld pool geometry and the experimentally measured geometry is presented in Fig. 9. The calculated results also show the temperature contours and the computed velocity field. The computed velocity field shows that the liquid metal is transported from the middle of the pool outwards to the periphery due to negative temperature coefficient of surface tension.

The values of $k^*$ and $\mu^*$ obtained in this work are in the range of enhancement factors reported in the literature. For example, an effective value of 30 for both $k^*$ and $\mu^*$ was reported to result in best prediction of GTA weld dimensions.[25] A value of 100 for both $k^*$ and $\mu^*$ was also indicated to be possible for welds with high depth of penetration.[25] When the $k-\epsilon$ turbulence model with a spatially varying effective viscosity was used, a maximum value of 16 for $\mu^*$ was reported for stationary GTA weld pool.[24] Although the relationships between $N_{HI}$ and $k^*$ and $\mu^*$ determined in this work are valid for the specific conditions of welding considered here, two important issues are to be noted. First, the values of both $k^*$ and $\mu^*$ are needed for phenomenological modeling, i.e., for the calculation of weld pool geometry and cooling rate using numerical heat transfer and fluid flow model. Second, because of organized research in recent years, there is now a growing quantitative knowledge base for fusion welding, consisting of data, mechanisms, models, rules, and laws applicable specifically for fusion welding. Significant expansion of this knowledge base is necessary for it to serve as a basis for the control of welding processes aimed at achieving defect free, structurally sound welds, and eventually transform welding to a mainstream engineering branch. The development of smart models of welding, that can determine uncertain welding parameters from a limited volume of experimental data, is a contribution toward expanding this quantitative knowledge base.

## V. SUMMARY AND CONCLUSIONS

A smart model embodying the Levenberg–Marquardt method of parameter estimation and three-dimensional numerical calculations of heat transfer and fluid flow is developed here for the estimation of effective thermal conductivity and effective viscosity in weld pool. Experimental data on weld penetration and width for six conduction mode laser welds were used. The computed weld dimensions were found to be sensitive to both the effective thermal conductivity and effective viscosity. It is found that the effective thermal conductivity and effective viscosity depended on the heat input. The optimum values of both effective thermal conductivity and effective viscosity were independent of their initial guessed values. However, their initial choice affected the volume of numerical calculations. The accuracy of the estimated values was verified using the numerical heat transfer and fluid flow model and the experimental data.

## ACKNOWLEDGMENTS

The work was supported by a grant from the U.S. Department of Energy, Office of Basic Energy Sciences, Division of Materials Sciences, under Grant No. DE-FGO2-01ER45900. Valuable critical comments from A. Kumar are appreciated.

## APPENDIX

In order to explain the basic concept for the optimization in details, a simplified system involving one dependent variable and two unknown parameters, $f_1$ and $f_2$, measured under six welding conditions is considered first. Equation (13) can be written for $f_1$ and $f_2$ as

$$\sum_{m=1}^{6}\left[(p_m^*-1)\frac{\partial p_m^*}{\partial f_1}\right]=0, \tag{A1}$$

$$\sum_{m=1}^{6}\left[(p_m^*-1)\frac{\partial p_m^*}{\partial f_2}\right]=0. \tag{A2}$$

The values of the two unknowns, $f_1$ and $f_2$, cannot be directly obtained from the earlier equations since they do not appear explicitly in these equations. However, the dependent variable $p_m^*$ can be expanded using the Taylor's series expansion to explicitly contain values of increments and $f_1$ and $f_2$. Considering two successive iterations of $p_m^*$ and taking only the first order terms

$$(p_m^*)^{k+1}=(p_m^*)^k+\frac{\partial(p_m^*)^k}{\partial f_1}\Delta f_1^k+\frac{\partial(p_m^*)^k}{\partial f_2}\Delta f_2^k, \tag{A3}$$

where $\Delta f_1^k$ and $\Delta f_2^k$ are two unknown increments of $f_1$ and $f_2$. All other terms on the right-hand side of Eq. (A3) are considered to be known. The value of $p_m^*$ at the end of $(k+1)$th iteration, $(p_m^*)^{k+1}$, is unknown since $\Delta f_1^k$ and $\Delta f_2^k$, and hence, $f_1$ and $f_2$ after $(k+1)$th iteration are unknown. It should be noted here that $p_m^*$ is always considered to be evaluated through the numerical heat transfer and fluid flow simulation using a corresponding set of $f_1$ and $f_2$ and other known parameters.

The Eqs. (A1) and (A2) are rewritten replacing $p_m^*$ by $(p_m^*)^{k+1}$ as

$$\sum_{m=1}^{6}\left\{[(p_m^*)^{k+1}-1]\frac{(\partial p_m^*)^{k+1}}{\partial f_1}\right\}=0, \tag{A4}$$

$$\sum_{m=1}^{6}\left\{[(p_m^*)^{k+1}-1]\frac{(\partial p_m^*)^{k+1}}{\partial f_2}\right\}=0. \tag{A5}$$

Substituting $(p_m^*)^{k+1}$ by the terms on the right-hand side of equation (A3), both equations (A4) and (A5) are rewritten as

$$\sum_{m=1}^{6}\left\{\left[(p_m^*)^k+\frac{\partial(p_m^*)^k}{\partial f_1}\Delta f_1^k+\frac{\partial(p_m^*)^k}{\partial f_2}\Delta f_2^k-1\right]\times\frac{\partial\left[(p_m^*)^k+\frac{\partial(p_m^*)^k}{\partial f_1}\Delta f_1^k+\frac{\partial(p_m^*)^k}{\partial f_2}\Delta f_2^k\right]}{\partial f_1}\right\}=0, \tag{A6}$$

$$\sum_{m=1}^{6}\left\{\left[(p_m^*)^k+\frac{\partial(p_m^*)^k}{\partial f_1}\Delta f_1^k+\frac{\partial(p_m^*)^k}{\partial f_2}\Delta f_2^k-1\right]\times\frac{\partial\left[(p_m^*)^k+\frac{\partial(p_m^*)^k}{\partial f_1}\Delta f_1^k+\frac{\partial(p_m^*)^k}{\partial f_2}\Delta f_2^k\right]}{\partial f_2}\right\}=0. \tag{A7}$$

Neglecting higher order differentials such as $\partial/\partial f_1\{[\partial(p_m^*)^k/\partial f_1]\Delta f_1^k\}$, Eqs. (A6) and (A7) are simplified as

$$\sum_{m=1}^{6}\left\{\left[(p_m^*)^k+\frac{\partial(p_m^*)^k}{\partial f_1}\Delta f_1^k+\frac{\partial(p_m^*)^k}{\partial f_2}\Delta f_2^k-1\right]\frac{\partial(p_m^*)^k}{\partial f_1}\right\}=0, \tag{A8}$$

$$\sum_{m=1}^{6}\left\{\left[(p_m^*)^k+\frac{\partial(p_m^*)^k}{\partial f_1}\Delta f_1^k+\frac{\partial(p_m^*)^k}{\partial f_2}\Delta f_2^k-1\right]\frac{\partial(p_m^*)^k}{\partial f_2}\right\}=0. \tag{A9}$$

Equations (A8) and (A9) can be rearranged as

$$\sum_{m=1}^{6}\left[\frac{\partial(p_m^*)^k}{\partial f_1}\frac{\partial(p_m^*)^k}{\partial f_1}\right]\Delta f_1^k+\sum_{m=1}^{6}\left[\frac{\partial(p_m^*)^k}{\partial f_1}\frac{\partial(p_m^*)^k}{\partial f_2}\right]\Delta f_2^k=-\sum_{m=1}^{6}\left\{\frac{\partial(p_m^*)^k}{\partial f_1}[(p_m^*)^k-1]\right\}, \tag{A10}$$

$$\sum_{m=1}^{6}\left[\frac{\partial(p_m^*)^k}{\partial f_2}\frac{\partial(p_m^*)^k}{\partial f_1}\right]\Delta f_1^k+\sum_{m=1}^{6}\left[\frac{\partial(p_m^*)^k}{\partial f_2}\frac{\partial(p_m^*)^k}{\partial f_2}\right]\Delta f_2^k=-\sum_{m=1}^{6}\left\{\frac{\partial(p_m^*)^k}{\partial f_2}[(p_m^*)^k-1]\right\}. \tag{A11}$$

Equations (A10) and (A11) can also be expressed as

$$S_{11}\Delta f_1^k+S_{12}\Delta f_2^k=-S_1^p, \tag{A12}$$

$$S_{21}\Delta f_1^k+S_{22}\Delta f_2^k=-S_2^p. \tag{A13}$$

Equations (A12) and (A13) can be expressed in a matrix form as

$$\begin{bmatrix}S_{11}&S_{12}\\S_{21}&S_{22}\end{bmatrix}\begin{Bmatrix}\Delta f_1^k\\\Delta f_2^k\end{Bmatrix}=-\begin{Bmatrix}S_1^p\\S_2^p\end{Bmatrix} \tag{A14}$$

or

$$[S]\{\Delta f^k\}=-\{S^*\}, \tag{A15}$$

where

$$[S]=\begin{bmatrix}S_{11}&S_{12}\\S_{21}&S_{22}\end{bmatrix}=\begin{bmatrix}\sum_{m=1}^{6}\frac{\partial(p_m^*)^k}{\partial f_1}\frac{\partial(p_m^*)^k}{\partial f_1}&\sum_{m=1}^{6}\frac{\partial(p_m^*)^k}{\partial f_1}\frac{\partial(p_m^*)^k}{\partial f_2}\\\sum_{m=1}^{6}\frac{\partial(p_m^*)^k}{\partial f_2}\frac{\partial(p_m^*)^k}{\partial f_1}&\sum_{m=1}^{6}\frac{\partial(p_m^*)^k}{\partial f_2}\frac{\partial(p_m^*)^k}{\partial f_2}\end{bmatrix} \tag{A16}$$

and

$$\{S^*\}=\begin{Bmatrix}S_1^p\\S_2^p\end{Bmatrix}=\begin{Bmatrix}\sum_{m=1}^{6}\frac{\partial(p_m^*)^k}{\partial f_1}[(p_m^*)^k-1]\\\sum_{m=1}^{6}\frac{\partial(p_m^*)^k}{\partial f_2}[(p_m^*)^k-1]\end{Bmatrix}. \tag{A17}$$

Thus, Eqs. (A1) and (A2) are modified to Eq. (A14) where the two unknown incremental terms $\Delta f_1^k$ and $\Delta f_2^k$ are explicitly defined in terms of known quantities. All other terms in Eq. (A14) are known at the end of $k$th iteration. The variables $\Delta f_1^k$ and $\Delta f_2^k$ are determined from the solution of Eq. (A14). The unknown parameters $f_1$ and $f_2$ after $(k+1)$th iteration are obtained from the following relations:

$$f_1^{k+1}=f_1^k+\Delta f_1^k,\qquad f_2^{k+1}=f_2^k+\Delta f_2^k. \tag{A18}$$

The updated values of $f_1^{k+1}$ and $f_2^{k+1}$ are used next to evaluate $(p_m^c)^{k+1}$ through the numerical heat transfer and fluid flow simulation. Next, $O(f)$ is calculated from the following equation:

$$O(f)=\sum_{m=1}^{6}[(p_m^*)^{k+1}-1]^2=0. \tag{A19}$$

The value of $O(f)$ calculated from Eq. (A19) is compared with that calculated previously after $k$th iteration. Values of $f_1$ and $f_2$ are assumed to have converged when the value of $O(f)$ calculated from Eq. (A19) after $(k+1)$th iterations is found to be smaller than a predefined small number.

For two dependent variables, $p_m^*$ and $w_m^*$, the expression (A16) is modified as

$$[S]=\begin{bmatrix}S_{11}&S_{12}\\S_{21}&S_{22}\end{bmatrix}, \tag{A20}$$

where

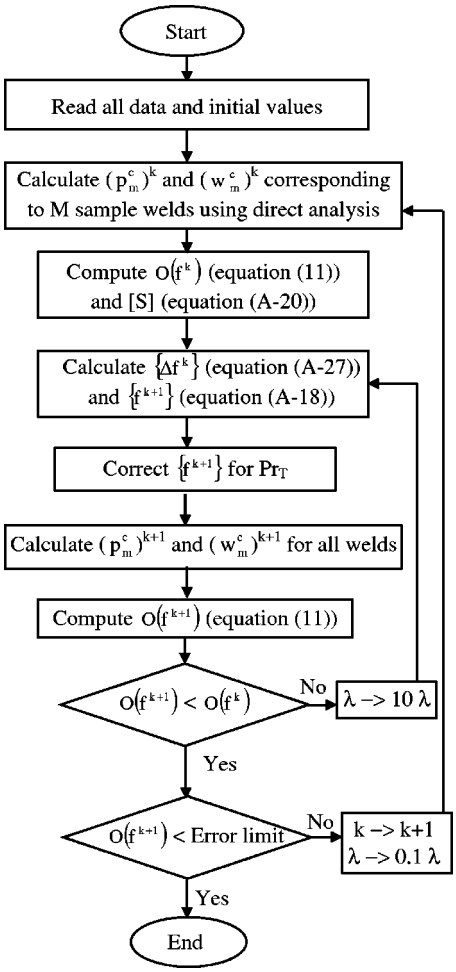


FIG. 10. Flow chart of the smart modeling procedure.

$$S_{ij}=\sum_{m=1}^{6}\left[\frac{\partial(p_m^*)^k}{\partial f_i}\frac{\partial(p_m^*)^k}{\partial f_j}+\frac{\partial(w_m^*)^k}{\partial f_i}\frac{\partial(w_m^*)^k}{\partial f_j}\right];$$

$$\text{for } i,j=1-2. \tag{A21}$$

The indices $i$ and $j$ refer to the number of unknown parameters. The expression (A17) will be modified as

$$\{S^*\}=\begin{Bmatrix} S_1^{pw} \\ S_2^{pw} \end{Bmatrix} \tag{A22}$$

with

$$S_i^{pw}=\sum_{m=1}^{6}\left\{\frac{\partial(p_m^*)^k}{\partial f_i}[(p_m^*)^k-1]+\frac{\partial(w_m^*)^k}{\partial f_i}[(w_m^*)^k-1]\right\};$$

$$\text{for } i=1-2. \tag{A23}$$

The unknown matrix $\{\Delta f^k\}$ in Eq. (A15) will remain same as

$$\{\Delta f^k\}=\begin{Bmatrix} \Delta f_1^k \\ \Delta f_2^k \end{Bmatrix}. \tag{A24}$$

The expression (A18) will also remain same as number of unknowns remains two only. Furthermore, the sensitivity terms such as $\partial(p_m^*)^k/\partial f_i$ or $\partial(w_m^*)^k/\partial f_i$ (for $i=1-2$) in the expressions (A16) as well as in (A21) often tend to be very small as the values of the unknown parameters $f_1$ and $f_2$ move close to the optimum values. As a result, the matrix $[S]$ may tend to become a singular matrix. To avoid any numerical instability, Eq. (A15) is further modified following the Levenburg–Marquardt method as

$$([S]+\lambda\mathbf{I})\{\Delta f^k\}=-\{S^*\}, \tag{A25}$$

where $\lambda$ is a scalar damping coefficient which is usually taken as 0.001. $\mathbf{I}$ is a diagonal matrix defined as[42]

$$\mathbf{I}=\begin{bmatrix} S_{11} & 0 \\ 0 & S_{22} \end{bmatrix}. \tag{A26}$$

Hence, Eq. (A25) can be rewritten as

$$\left(\begin{bmatrix} S_{11} & S_{12} \\ S_{21} & S_{22} \end{bmatrix}+\lambda\begin{bmatrix} S_{11} & 0 \\ 0 & S_{22} \end{bmatrix}\right)\begin{Bmatrix} \Delta f_1^k \\ \Delta f_2^k \end{Bmatrix}=-\begin{Bmatrix} S_1^p \\ S_2^p \end{Bmatrix}. \tag{A27}$$

The order of $\mathbf{I}$ will always be same as that of the matrix $[S]$. Thus, the product $\lambda\mathbf{I}$ in Eq. (A25) ensures that the left hand term in Eq. (A26) will remain nonzero even if the determinant of the matrix $[S]$ is zero. The sequence of steps involved in the modeling is shown in Fig. 10.


[1] S. A. David and T. DebRoy, Science **257**, 497 (1992).
[2] T. DebRoy and S. A. David, Rev. Mod. Phys. **67**, 85 (1995).
[3] H. Zhao, D. R. White, and T. DebRoy, Int. Mater. Rev. **44**, 238 (1999).
[4] K. Mundra, T. DebRoy, and K. M. Kelkar, Numer. Heat Transfer, Part A **29**, 115 (1996).
[5] J. W. Elmer, T. A. Palmer, W. Zhang, B. Wood, and T. DebRoy, Acta Mater. **51**, 3333 (2003).
[6] S. Kou and Y. H. Wang, Metall. Mater. Trans. A **17**, 2265 (1986).
[7] W. Pitscheneder, T. DebRoy, K. Mundra, and R. Ebner, Weld. J. (Miami, FL, U. S.) **75**, 71s (1996).
[8] W. Zhang, J. W. Elmer, and T. DebRoy, Mater. Sci. Eng., A **333**, 320 (2002).
[9] T. Cool and H. K. D. H. Bhadeshia, Sci. Technol. Weld. Joining **2**, 36 (1997).
[10] Z. Yang, J. W. Elmer, J. Wang, and T. DebRoy, Weld. J. (Miami, FL, U. S.) **79**, 97s (2000).
[11] Z. Yang, S. Sista, J. W. Elmer, and T. DebRoy, Acta Mater. **48**, 4813 (2000).
[12] T. Hong, W. Pitscheneder, and T. DebRoy, Sci. Technol. Weld. Joining **3**, 33 (1998).
[13] S. S. Babu, S. A. David, K. Mundra, and T. DebRoy, Mater. Sci. Technol. **11**, 186 (1995).
[14] T. Hong and T. DebRoy, Ironmaking Steelmaking **28**, 450 (2001).
[15] K. Mundra and T. DebRoy, Metall. Trans. B **24B**, 145 (1993).
[16] H. Zhao and T. DebRoy, Metall. Mater. Trans. B **32B**, 163 (2001).
[17] T. A. Palmer and T. DebRoy, Metall. Mater. Trans. B **31B**, 1371 (2000).
[18] K. Mundra, J. M. Blackburn, and T. DebRoy, Sci. Technol. Weld. Joining **2**, 174 (1997).
[19] X. He, P. W. Fuerschbach, and T. DebRoy, J. Phys. D **36**, 1388 (2003).
[20] H. Zhao and T. DebRoy, J. Appl. Phys. **93**, 10089 (2003).
[21] W. Zhang, G. G. Roy, J. W. Elmer, and T. DebRoy, J. Appl. Phys. **93**, 3022 (2003).
[22] A. Kumar and T. DebRoy, J. Appl. Phys. **94**, 1267 (2003).
[23] C. H. Kim, W. Zhang, and T. DebRoy, J. Appl. Phys. **94**, 2667 (2003).
[24] K. Hong, D. C. Weckmann, A. B. Strong, and W. Zheng, Sci. Technol. Weld. Joining **7**, 125 (2002).
[25] R. T. C. Choo and J. Szekely, Weld. J. (Miami, FL, U. S.) **73**, 25s (1994).
[26] P. G. Jonsson, J. Szekely, R. T. C. Choo, and T. P. Quinn, Modell. Simul. Mater. Sci. Eng. **2**, 995 (1994).
[27] A. De and T. DebRoy, J. Phys. D **37**, 140 (2004).
[28] A. Paul and T. DebRoy, Metall. Trans. B **19B**, 851 (1988).
[29] Z. Yang and T. DebRoy, Metall. Mater. Trans. B **30B**, 483 (1999).
[30] Y. F. Hsu, B. Rubinsky, and K. Mahin, J. Heat Transfer **108**, 734 (1986).
[31] J. V. Beck, in *Modeling of Casting, Welding and Advanced Solidification Processes V*, edited by M. Rappaz *et al.* (The Minerals, Metals and Materials Society, Warrendale, PA, 1991), p. 503.
[32] M. Rappaz, J.-L. Desbiolles, J.-M. Drezet, Ch.-A. Gandin, A. Jacot, and

PH. Thevoz, in *Modeling of Casting, Welding and Advanced Solidification Processes VII*, edited by M. Cross *et al.* (The Minerals, Metals and Materials Society, Warrendale, PA, 1995), p. 449.
[33] R. W. Fonda and S. G. Lambrakos, Sci. Technol. Weld. Joining **7**, 177 (2002).
[34] V. A. Karkhin, V. V. Plochikhine, and H. W. Bergmann, Sci. Technol. Weld. Joining **7**, 224 (2002).
[35] W. Pitscheneder, Ph.D. thesis, University of Leoben, Austria, 2001.
[36] S. V. Patankar, *Numerical Heat Transfer and Fluid Flow* (McGraw-Hill, New York, 1982).
[37] V. R. Voller and C. Prakash, Int. J. Heat Mass Transfer **30**, 1709 (1987).
[38] A. D. Brent, V. R. Voller, and K. J. Reid, Numer. Heat Transfer **13**, 297 (1988).
[39] T. DebRoy, A. K. Mazumdar, and D. B. Spalding, Appl. Math. Model. **2**, 146 (1978).
[40] J. V. Beck and K. J. Arnold, *Parameter Estimation in Engineering and Science* (Wiley, New York, 1977).
[41] J. V. Beck, B. Blackwell, and C. R. Clair, Jr., *Inverse Heat Conduction—Ill Posed Problems* (Wiley, New York, 1985).
[42] M. N. Ozisik and H. R. B. Orlande, *Inverse Heat Transfer* (Taylor & Francis, New York, 2000).